The Astrophysical Journal, 775:20 (13pp), 2013 September 20 doi:10.1088/0004-637X/775/1/20

THE RICH GLOBULAR CLUSTER SYSTEM OF ABELL 1689 AND THE RADIAL DEPENDENCE OF THE GLOBULAR CLUSTER FORMATION EFFICIENCY

K. A. Alamo-Martínez[1,2], J. P. Blakeslee[2], M. J. Jee[3], P. Côté[2], L. Ferrarese[2], R. A. González-Lópezlira[1], A. Jordán[4], G. R. Meurer[5], E. W. Peng[6], and M. J. West[7,8]

[1] Centro de Radioastronomía y Astrofísica, Universidad Nacional Autónoma de México, Morelia 58090, Mexico; k.alamo@crya.unam.mx
[2] Herzberg Institute of Astrophysics, National Research Council of Canada, Victoria, BC V9E 2E7, Canada
[3] Department of Physics, University of California, Davis, One Shields Avenue, Davis, CA 95616, USA
[4] Departamento de Astronomía y Astrofísica, Pontificia Universidad Católica de Chile, 7820436 Macul, Santiago, Chile
[5] International Centre for Radio Astronomy Research, The University of Western Australia, 35 Stirling Highway, Crawley, WA 6009, Australia
[6] Department of Astronomy and Kavli Institute for Astronomy and Astrophysics, Peking University, Beijing 100871, China
[7] European Southern Observatory, Alonso de Córdova 3107, Vitacura, Santiago, Chile
[8] Maria Mitchell Observatory, 4 Vestal Street, Nantucket, MA 02554, USA
Received 2013 May 8; accepted 2013 July 24; published 2013 August 30

ABSTRACT

We study the rich globular cluster (GC) system in the center of the massive cluster of galaxies Abell 1689 ($z = 0.18$), one of the most powerful gravitational lenses known. With 28 *Hubble Space Telescope*/Advanced Camera for Surveys orbits in the F814W bandpass, we reach a magnitude $I_{814} = 29$ with $\gtrsim$90% completeness and sample the brightest ∼5% of the GC system. Assuming the well-known Gaussian form of the GC luminosity function (GCLF), we estimate a total population of $N_{\rm GC}^{\rm total} = 162{,}850^{+75{,}450}_{-51{,}310}$ GCs within a projected radius of 400 kpc. As many as half of the GCs may comprise an intracluster component. Even with the sizable uncertainties, which mainly result from the uncertain GCLF parameters, this system is by far the largest GC population studied to date. The specific frequency S_N is high, but not uncommon for central galaxies in massive clusters, rising from $S_N \approx 5$ near the center to ∼12 at large radii. Passive galaxy fading would increase S_N by ∼20% at $z = 0$. We construct the radial mass profiles of the GCs, stars, intracluster gas, and lensing-derived total mass, and we compare the mass fractions as a function of radius. The estimated mass in GCs, $\mathcal{M}_{\rm GC}^{\rm total} = 3.9 \times 10^{10}\,M_\odot$, is comparable to ∼80% of the total stellar mass of the Milky Way. The shape of the GC mass profile appears intermediate between those of the stellar light and total cluster mass. Despite the extreme nature of this system, the ratios of the GC mass to the baryonic and total masses, and thus the GC formation efficiency, are typical of those in other rich clusters when comparing at the same physical radii. The GC formation efficiency is not constant, but varies with radius, in a manner that appears similar for different clusters; we speculate on the reasons for this similarity in profile.

Key words: galaxies: clusters: individual (Abell 1689) – globular clusters: general

Online-only material: color figures

1. INTRODUCTION

In the usual hierarchical structure formation model, pregalactic objects begin forming through gravitational instability in high-density regions and coalesce to form progressively larger structures (e.g., Springel et al. 2005; De Lucia et al. 2006). Massive clusters of galaxies, the largest self-gravitating systems in the universe today, saw the earliest major star formation and have been assembling for the longest time. The rapid merging and accretion in these dense environments has obscured much information about their early dynamical histories. However, high-resolution numerical simulations indicate that old metal-poor globular clusters (GCs) and diffuse stellar light provide reliable tracers of the earliest star-forming substructures (Moore et al. 2006; Abadi et al. 2006), including their spatial distributions and kinematics. In contrast, the surviving dwarf satellites likely originated at lower densities and were accreted later (see Font et al. 2006; De Lucia & Helmi 2008; Johnston et al. 2008).

GCs are especially useful tracers because they are abundant in all large galaxies and most dwarfs with masses of at least $10^8\,M_\odot$ (e.g., Peng et al. 2008). As in the Milky Way, they generally have ages $\gtrsim$10 Gyr and peak metallicities just a few percent of solar (e.g., Cohen et al. 1998, 2003; Puzia et al. 2005; Chies-Santos et al. 2011, 2012), consistent with their being relicts of early accretion. Harris & van den Bergh (1981) introduced the specific frequency S_N (the number of GCs per unit galaxy luminosity) as a normalized measure of population richness. S_N has been measured for galaxies of all morphological types and environments (see reviews by Harris 1991, 2001; West et al. 2004; Brodie & Strader 2006), although it has been most commonly measured in early-type galaxies as spirals generally have much sparser GC systems. For early-type dwarfs, S_N exhibits a large scatter, with values ranging from 0 to ∼100, and some tendency to increase as the luminosity decreases. Conversely, for more luminous ellipticals, S_N ranges from ∼2 to ∼10 and tends to increase with luminosity.

Similar trends of S_N with luminosity occur for early-type galaxies in both clusters and isolated environments (e.g., Cho et al. 2012; Alamo-Martínez et al. 2012). The exception is for galaxies near the dynamical centers of massive clusters, where the total GC population often exceeds 10,000 and the central cD galaxy may have $S_N > 10$ (Harris et al. 1995; West et al. 1995). Blakeslee et al. (1997) found that the number $N_{\rm GC}$ of GCs in such systems scales approximately with cluster velocity dispersion, X-ray luminosity, and other indicators of cluster mass, rather than with host galaxy luminosity. Thus, the number per unit total (halo) mass shows much less variation than S_N. McLaughlin (1999) found a similar scaling of $N_{\rm GC}$ in massive ellipticals with baryonic mass; Blakeslee (1999) showed that the ratio of the scale factors was consistent with

the expected baryon fraction. Numerical models also predict an approximately constant frequency of old metal-poor GCs relative to total halo mass, depending on the degree of local variation in the epoch of reionization (Moore et al. 2006).

Peng et al. (2008) studied S_N and the stellar mass fraction contained in GCs for 100 early-type galaxies from the Advanced Camera for Surveys (ACS) Virgo Cluster Survey (Côté et al. 2004). These authors found that the GC stellar mass fraction tends to be larger in giant and dwarf galaxies, but is universally low at intermediate masses. Such intermediate-mass galaxies also appear to have been most efficient at converting baryons into stars (e.g., van den Bosch et al. 2007; Conroy & Wechsler 2009; Guo et al. 2010). Thus, as previously found for central cluster galaxies, the S_N and GC stellar mass fraction for the ensemble of Virgo galaxies scale more closely with halo mass (mainly dark matter) than with the stellar mass or luminosity. The observed variations therefore indicate a variable field star formation efficiency following the GC formation epoch. Spitler & Forbes (2009) compiled a sample of galaxies with a wide range of masses in various environments and also concluded that there was a direct proportionality between the mass in GCs and the total halo mass. Following this idea, Georgiev et al. (2010) studied GC formation efficiencies within an analytical model that included mass-dependent feedback mechanisms. They found that the GC formation efficiency is roughly constant with halo mass, but S_N and stellar mass fraction vary with the field star formation efficiency, which in turn depends on halo mass and is highest at intermediate values. In this model, the increased scatter among dwarf galaxies was attributed to stochastic effects at low mass. However, Peng et al. found that the Virgo dwarfs with high GC mass fractions were nearly all within 1 Mpc of the central cluster galaxy M87, indicating that location plays a key role in determining the relative fractions of baryons in GCs and field stars in these systems. This result could also be a consequence of the formation epoch, with GC formation efficiency being higher at early times (e.g., Kruijssen 2012).

In the Coma cluster, Peng et al. (2011) found a very large population of intracluster globular clusters (IGCs), which are bound to the cluster potential rather than to individual galaxies. Limits on the amount of diffuse intracluster light imply a high S_N for the IGC population, similar to the values for high-S_N cD galaxies and the centrally located Virgo dwarfs. IGCs appear to be a common feature of galaxy clusters: a significant population likely resides in A1185 (Jordán et al. 2003; West et al. 2011), a cluster in which the cD galaxy is offset from the centroid of X-ray emission; Lee et al. (2010) also report evidence for IGCs in Virgo. The IGC populations are overwhelmingly metal poor, with colors typical of GCs in dwarf galaxies and the outer regions of massive galaxies. Because of their early formation and subsequent dissipationless assembly, the spatial density profile of the IGCs is expected to trace the total cluster mass profile. However, because of their low surface densities and contamination from GCs bound to galaxies, it remains unclear whether IGCs follow more closely the stellar light, the baryonic matter (including the X-ray gas), or the dark matter distribution. Observations thus far have been limited to nearby ($z \lesssim 0.05$) moderate mass clusters. Further progress requires studying massive clusters with many thousands of GCs and well characterized baryonic and total mass density profiles.

Abell 1689 (hereafter A1689) is an extremely massive galaxy cluster at $z = 0.183$ with a velocity dispersion $\sigma \gtrsim 1400\,\mathrm{km\,s^{-1}}$ and complex kinematical substructure (e.g., Teague et al. 1990; Girardi et al. 1997; Lemze et al. 2009). It has one of the largest known Einstein radii, and its mass distribution has been extensively studied from both strong and weak lensing (Tyson & Fischer 1995; Taylor et al. 1998; Broadhurst et al. 2005, Zekser et al. 2006; Limousin et al. 2007; Coe et al. 2010), as well as X-ray properties (Andersson & Madejski 2004; Lemze et al. 2008). A recent multi-wavelength analysis by Sereno et al. (2013), including Sunyaev–Zeldovich, X-ray, and lensing data, finds a total mass $M_{200} = (1.3 \pm 0.2) \times 10^{15}\,M_\odot$ within $r_{200} = 2.1$ Mpc.

A1689 was one of the targets selected for early release observations with the ACS Wide Field Channel (ACS/WFC; Ford et al. 2002, 2003) after installation on the *Hubble Space Telescope* (*HST*). In addition to the strong lensing analyses referenced above, the same observations were used to investigate ultra-compact dwarf galaxies in an extremely rich environment (Mieske et al. 2004). Further inspection of these early ACS data revealed a concentration of faint point sources that were consistent with GCs at the distance of A1689. Assuming the usual Gaussian GC luminosity function (GCLF) implied a huge population of $\gtrsim 10^5$ GCs (Blakeslee 2005), but the number was very uncertain as it involved an extrapolation by two orders of magnitude.

Here, we report results from very deep *HST*/ACS observations of A1689 obtained in order to test the previous uncertain results and study the GC population in the center of this extraordinary cluster. The following section summarizes the observations and image reductions. Section 3 describes the photometric analysis of the galaxies and GCs in detail, while Section 4 presents our results of the GC number density distribution, total population, and specific frequency. In Section 5, we compare our results on the GC and galaxy light distributions with the mass profiles of the X-ray emitting gas and dark matter. The final section discusses our conclusions. Throughout this work, we adopt the *WMAP7* maximum likelihood cosmology (Komatsu et al. 2011) with $(h, \Omega_m, \Omega_\lambda) = (0.704, 0.27, 0.73)$, which yields a distance modulus for A1689 of $(m-M) = 39.74$ mag and a physical scale of 3.07 kpc arcsec^{-1} (these numbers change by $<0.5\%$ for the *WMAP9* cosmology of Hinshaw et al. 2012).

2. OBSERVATIONS AND IMAGE REDUCTION

As part of *HST* Program GO-11710, we imaged the central field of A1689 for 28 orbits with the F814W bandpass (also referred to as I_{814}) of the ACS/WFC during seven visits from 2010 May 29 to 2010 July 8. The charge transfer efficiency (CTE) of the ACS/WFC detectors has significantly degraded in recent years. After standard Space Telescope Science Institute pipeline processing to the point of calibrated "flt files," we therefore used the stand-alone script version of the empirical pixel-based CTE correction algorithm of Anderson & Bedin (2010) on each of the 56 individual exposures in our program. This correction script did an excellent job of removing the CTE trails in the data.

The individual exposures were then processed with Apsis (Blakeslee et al. 2003) to produce a single geometrically corrected, cosmic-ray cleaned, stacked image with a total exposure time of 75,172 s. At nearly 21 hr, this image is the single deepest ACS/WFC observation in the F814W bandpass. After experimenting with different Drizzle (Fruchter & Hook 2002) parameters within Apsis, we adopted the Gaussian interpolation kernel with a "pixfrac" of 0.5 and an output pixel scale of $0\farcs033$ pixel^{-1}. This set of parameters provides improved resolution with good

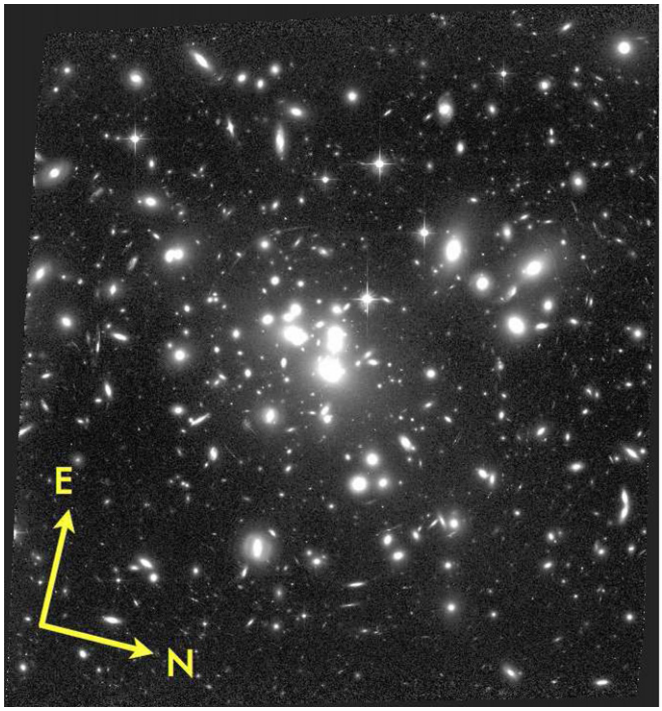

Figure 1. Deep ACS/WFC F814W image of the galaxy cluster A1689 from Program GO-11710, shown in the observed orientation. The field of view is $\sim 3\farcm3 \times 3\farcm3$.

(A color version of this figure is available in the online journal.)

sampling of the point spread function (PSF), without introducing excessive small-scale correlations in the pixel noise.

We calibrated the photometry in the AB system, using the F814W zero point of 25.947 determined from the time-dependent ACS Zeropoint Calculator.[9] The I_{814}-band Galactic extinction in the direction of A1689 is 0.04 mag (Schlafly & Finkbeiner 2011).

3. ANALYSIS

3.1. Galaxy Modeling

As one of the few richness class 4 clusters in the Abell catalog (Abell et al. 1989), A1689 is exceptionally rich in galaxies, particularly in its central region (Figure 1), a fact that hampers source detection and photometry. In order to obtain an image with the flattest background possible, we used the *ellipse* (Jedrzejewski 1987) and *bmodel* tasks within IRAF (Tody 1986, 1993) to construct isophotal models for 59 of the brightest galaxies in the ACS/WFC field. Neighboring galaxies were masked during the fitting and, in cases with very close companions, it was necessary to perform several iterations.

The isophotal models for the 59 galaxies were combined to produce a single *bmodel* image, which was then subtracted from the original image to create a first-pass residual image. SExtractor (Bertin & Arnouts 1996) was then run on this residual image to generate a map of the background due to the imperfect subtraction of the galaxies, as well as approximate representations of other unmodeled cluster galaxies. The SExtractor background map was then combined with the *ellipse*/*bmodel* models to produce our final luminosity model, which was subtracted from the original image to obtain what we refer to as the "final_residual" image.

[9] http://www.stsci.edu/hst/acs/analysis/zeropoints

3.2. Object Detection

The final_residual image includes many smaller galaxies and residuals from larger galaxies that were difficult to model and not well represented by the SExtractor background map. To remove these smaller (but resolved) structures, a very smooth image was created with the IRAF task *rmedian* (a ring median filter with inner and outer radii of 5 and 9 pixels, respectively) applied to the final_residual image. This ring-median image was then subtracted from the final_residual to obtain the "rmed_residual" image (Figure 2). Although the rmed_residual image is extremely flat and suitable for point source detection, it cannot be used to measure reliable source magnitudes as some flux is removed by the rmedian process.

The source detection was performed with SExtractor on the rmed_residual image. In order to make the detection more robust, we used an rms error image for the SExtractor detection WEIGHT map, produced as described by Jordán et al. (2004). This rms map includes detector and photometric noise, as well as the signal-to-noise variations from the corrected bad pixels and cosmic rays. Bright stars, diffraction spikes, areas of lower exposure time near the image edges, and regions with large model residuals (due to sharp or irregular features within the cluster galaxies) were masked during the detection (black regions in Figure 3, right panel). At a luminosity distance of 885 Mpc, the GCs appear as point sources and the SExtractor parameters were chosen to optimize point source detection, using a threshold of 5 or more connected pixels at least 1.5σ above the local background.

Source magnitudes were measured in the final_residual image with PSF photometry, using the SExtractor output coordinates. The PSF photometry is more accurate than the various aperture magnitudes measured by SExtractor. The PSF was constructed using the standard DAOPHOT (Stetson 1987) procedure. The important parameters were the FWHM of the PSF fwhmpsf = 2.6 pixels ($0\farcs086$), aperture = 4 pixels, and varorder = 2, which means that the PSF is quadratically variable over the image. The best-fitting function to describe the PSF was *penny1*.[10] Since the radius of the PSF model is finite, an aperture correction, $m_{\rm apcor}$, was estimated. To this end, first the magnitude difference between 4 and 15 pixels ($\sim 0\farcs5$) was measured, then a correction from an aperture of $0\farcs5$ to infinity was obtained from Sirianni et al. (2005). The final aperture correction $m_{\rm apcor} = -0.36$ mag was applied to all the measured DAOPHOT fit magnitudes.

3.3. GC Candidate Selection

The DAOPHOT parameters $\chi_{\rm DAO}$ and $sharp_{\rm DAO}$, which gauge the goodness of the PSF fit and profile sharpness for each object, together provide a good indication of whether an object is a point source. Based on input and output parameters of artificial stars constructed from the PSF, we selected point sources as objects with $\chi_{\rm DAO} < 5$ and $-0.9 < sharp_{\rm DAO} < 0.9$.

Assuming that the GCs in A1689 are similar to nearby GCs, they should appear at $I_{814} \gtrsim 27.0$ AB. We therefore selected GC candidates as point sources having $27.0 < I_{814} < 29.32$; the faint limit is the magnitude where our detection is 50% complete in the innermost region of the cluster (see below). From this combined selection, we obtained a sample of 8212 GC candidates; Figure 3 shows their x, y positions, which are strongly concentrated near the cD galaxy; excesses of

[10] An elliptical Gaussian core that can be tilted at an arbitrary angle, with Lorentzian wings.

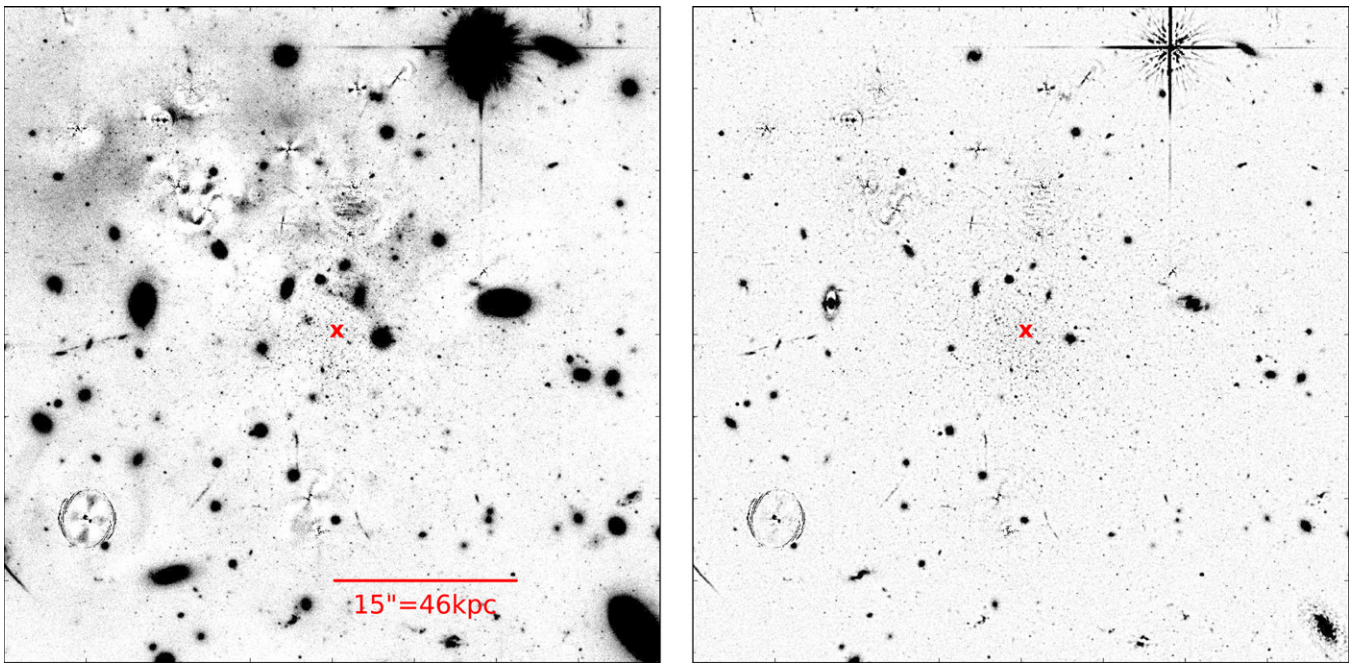

Figure 2. Zoom-in on the central region (∼160 × 160 kpc) of A1689. The red cross marks the center of the cD galaxy. Left panel: residual after subtraction of the luminosity model (*bmodel* plus SExtractor background map); because of its shallow light profile, the cD galaxy itself subtracts very well. Right panel: residual after subtraction of the luminosity model and the smooth rmedian image, used only for object detection.

(A color version of this figure is available in the online journal.)

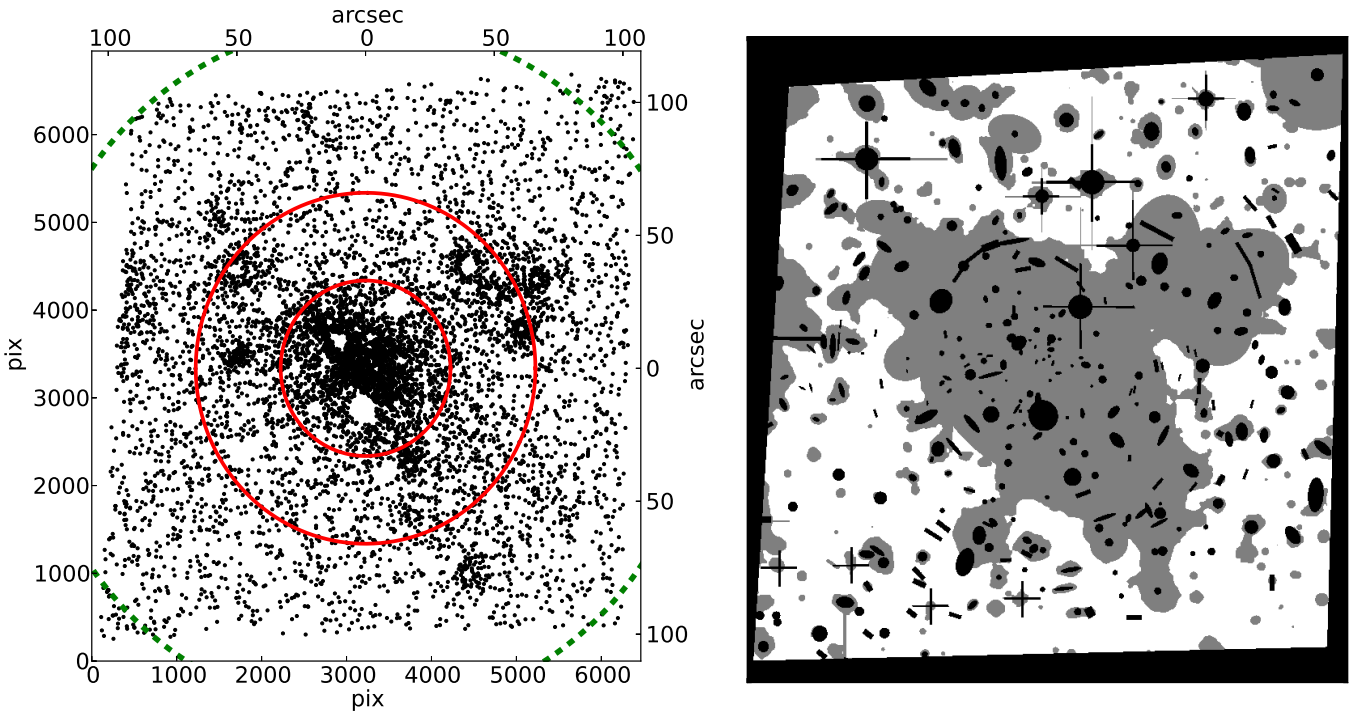

Figure 3. Left panel: spatial distribution of GC candidates; the red circles mark the boundaries of the three separate regions where the completeness function was fit and the green dashed circle indicates a radius of 400 kpc (130″). Right panel: black regions indicate the areas masked throughout the entire analysis; the gray regions show the masks applied for the galaxies, including the cD galaxy, used in estimating the number of background contaminants *bg* (see Section 3.5).

(A color version of this figure is available in the online journal.)

GC candidates are also visible around other cluster galaxies as well.

3.4. Completeness

To quantify the completeness, 250,000 artificial stars were constructed from the PSF model and added 500 at a time with random r, θ positions. The origin of the polar coordinates was the center of the cD galaxy, and the uniform random distribution in r yielded a higher density of sources near the cluster center, mimicking the actual sources. In adding the artificial sources, the masked areas were avoided and the added sources were not allowed to overlap with each other. The artificial stars

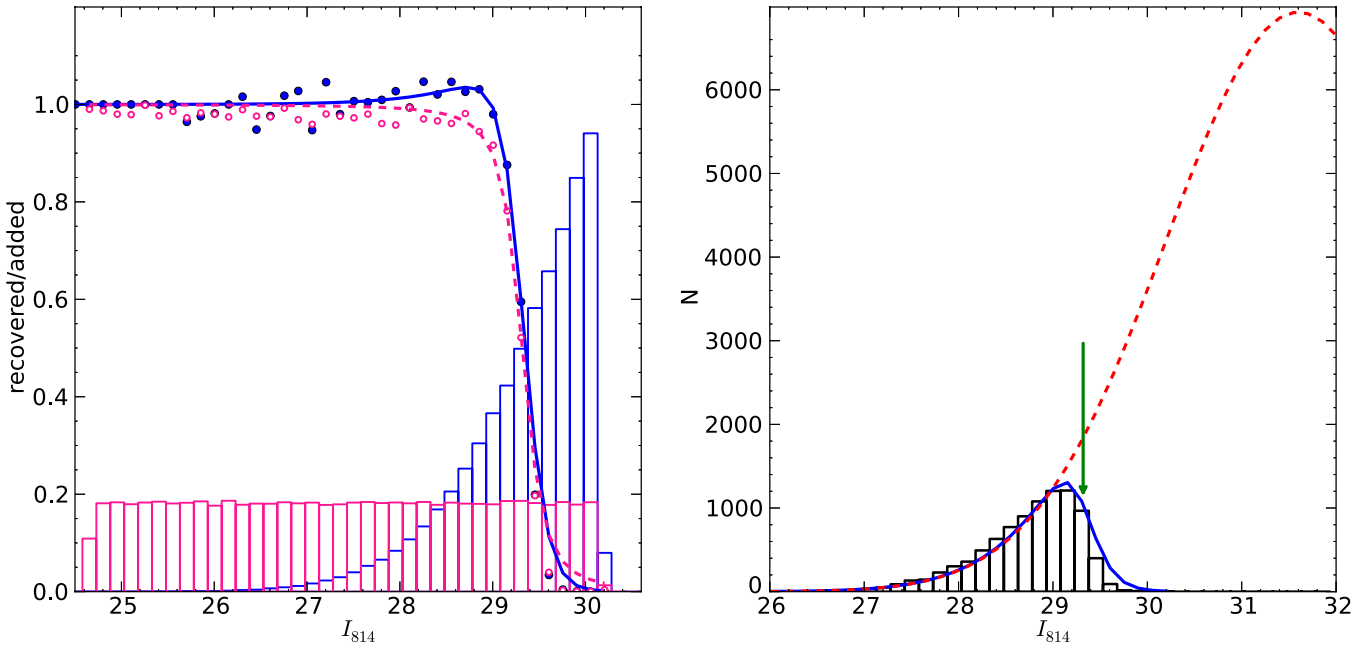

Figure 4. Left panel: completeness functions for the two different input magnitude distributions. Histograms: magnitude distributions of the artificial stars, i.e., a Gaussian with mean $\mu = 31.6$ mag and $\sigma = 1.5$ mag (blue) and uniform (pink). The blue points and pink open circles are the respective recovered fractions and the lines show the respective best-fit completeness functions: Pritchet (dashed pink) and modified Fermi (solid blue). The rising Gaussian distribution, meant to mimic the actual GCLF, causes an excess of recovered point sources near the completeness limit because of the Eddington bias. Right panel: observed luminosity function of GC candidates (histogram); fitted modified Fermi function × Gaussian model (solid blue line); and the derived Gaussian GCLF (dashed red line). The green arrow at $I_{814} = 29.32$ indicates the magnitude limit used for the fits.

(A color version of this figure is available in the online journal.)

were added to the rmed_residual and final_residual images and their fluxes were measured with the same procedure that was followed for the real objects, including the selection based on the values of $\chi_{\rm DAO}$ and $sharp_{\rm DAO}$. We carried out this whole process twice, using two different magnitude distributions for the artificial sources: (1) a uniform, or box-shaped, distribution with $25.0 < m < 30.5$ and (2) a Gaussian distribution with mean $\mu = 31.6$, $\sigma = 1.5$, and the constraint $m < 30.5$ (more than a magnitude beyond the completeness limit). The latter case approximates the expected GCLF in A1689 (see Section 4); both distributions are illustrated in Figure 4.

In the case of the uniform magnitude distribution, the fraction of recovered stars as a function of magnitude is well described by a function of the form:

$$f^P(m) = \frac{1}{2}\left[1 - \frac{\alpha(m - m_{\rm lim})}{\sqrt{1 + \alpha^2(m - m_{\rm lim})^2}}\right], \quad (1)$$

where $m_{\rm lim}$ is the magnitude at which the completeness is 0.5 and α determines the steepness of the curve. This function f^P is sometimes referred to as a "Pritchet function" (e.g., McLaughlin et al. 1994).

In the case of the Gaussian magnitude distribution, the fraction of recovered stars actually exceeds unity before the steep drop in completeness sets in. This excess of detected sources is due to the Eddington (1913) bias: as a result of the steeply rising luminosity function, measurement errors cause more faint sources to be scattered to brighter detection magnitudes and relatively fewer bright sources to be scattered to fainter levels. In this case, including both magnitude bias and incompleteness, the recovered fraction was not well described by Equation (1). However, we found that it could be represented by the following modified version of the Fermi function:

$$f^F(m) = \frac{1 + C\exp\left[b(m - m_0)\right]}{1 + \exp\left[a(m - m_0)\right]}, \quad (2)$$

where m_0 is the magnitude at which the completeness would be 0.5 for a standard Fermi function ($C \equiv 0$). The other parameters are linked, but in rough terms; a controls the steepness of the cutoff, b (which must be $< a$) affects where the departure above unity begins, and C determines the amplitude of the departure.

Although the Pritchet function and uniform magnitude distributions are widely used in the literature, our analysis indicates that these assumptions require great caution: when the actual counts follow a steeply rising luminosity function, incompleteness corrections based on a uniform magnitude distribution overestimate the number of real sources. We adopt the results from the artificial star tests with the Gaussian magnitude distribution, since this distribution more closely approximates the expected GCLF. The magnitude distribution of background sources is also a rising function, more similar to the bright side of the Gaussian distribution than to the uniform distribution.

The ratios of recovered to added artificial stars as a function of recovered magnitude were calculated and a modified Fermi function was fit to the completeness fractions in three annular regions: from 0 to 33″, from 33″ to 1.′1, and beyond 1.′1 (red circles in Figure 3). The values of m_0 found for these three regions are 29.30, 29.35, and 29.33 mag, respectively. After applying the completeness corrections, the number of GC candidates brighter than our adopted limit $I_{814} < 29.32$ increases from 8212 to 8710 ± 100, or 6%. Had we used the completeness estimates based on the uniform magnitude distribution, the increase would instead have been 14%, overestimating the final GC number by 7.5%.

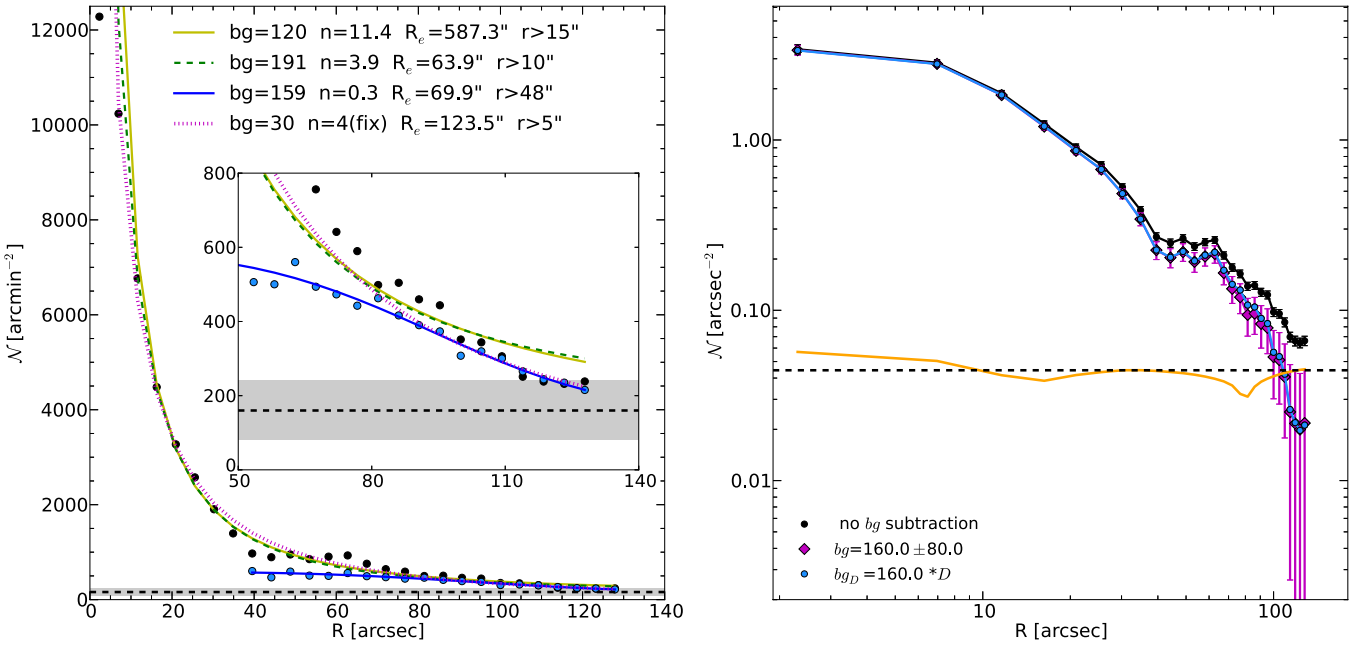

Figure 5. Radial distribution of the surface number density of GC candidates. Left panel: number of GC candidates per arcmin^2 (black dots). The dotted magenta, dashed green, and solid yellow lines show fitted Sérsic functions for different radial domains with the background (bg) as an additional free parameter. The blue dots are similar to the black ones, but obtained after all the bright galaxies have been masked; the blue line shows the corresponding Sérsic fit. The Sérsic parameters of the various fits are shown at the top. The dashed black line and gray shaded region indicate the final adopted background and 1σ error: $bg = (160 \pm 80)$ arcmin^{-2}. Inset: zoom-in of the outer parts of all the fits. Right panel: logarithmic plot of the number of GC candidates per arcsec^2 without background subtraction (black dots), after subtracting a constant density of 160 arcmin^{-2} (magenta diamonds), and after subtracting $160 \times D$ arcmin^{-2} (blue dots), where D represents the expected profile of the background dilution over this magnitude range as a result of the lens magnification (see the text). The dashed black line indicates a value of 160 arcmin^{-2}, while the solid orange line indicates $160 \times D$ arcmin^{-2}.

(A color version of this figure is available in the online journal.)

3.5. Background Contamination

To estimate the number of background contaminants bg, we first calculate the number of GC candidates per unit area as a function of radius (Figure 5). Then, we fit a Sérsic function (Sérsic 1968) plus the background bg as a free parameter to the surface number density profile $\mathcal{N}(r)$:

$$\mathcal{N}(r) = \mathcal{N}_e \exp\left\{-b_n\left[\left(\frac{r}{R_e}\right)^{1/n} - 1\right]\right\} + bg, \qquad (3)$$

where R_e is the effective radius that encloses half of the GC sample, $\mathcal{N}_e$ is $\mathcal{N}$ at R_e, n is the Sérsic index that controls the shape of the profile, and $b_n \approx 1.9992n - 0.3271$ (Graham & Driver 2005).

We found that the fitted Sérsic parameters and background were very sensitive to the radial range of the fit. This result is partly because of deviations from a smooth profile, but also because the number density of sources continues to decrease as a function of radius, without reaching a constant level. However, the mean background within our adopted magnitude limits must be in the range $0 < bg \lesssim 240$ arcmin^{-2} (the high value being the observed density in the outermost bins). After trying various radial cuts, we found the most robust value of bg resulted from masking the regions around all the bright galaxies (gray region in the right panel of Figure 3, based on our luminosity model). This procedure removes the concentrations of point sources associated with individual galaxies; the remaining objects follow a shallower, smoother radial density profile, shown in the left panel of Figure 5. The fitted background in this case was $bg \approx 160$ arcmin^{-2}, which was within the broad range returned by the various fits prior to the galaxy masking (see examples in the left panel of Figure 5). We adopt a conservative uncertainty of ±80 arcmin^{-2}, where the error bar encompasses the unlikely case that all objects in the outermost radial bins are background objects.

We note that after masking the bright galaxies, the remaining objects (blue points in the left panel of Figure 5) may represent a smooth population of IGCs in A1689. If we integrate the Sérsic function for these putative IGCs over the full area of the image (including the masked regions, since IGCs would also be projected onto the galaxies), we find that 50% of the GC candidates are in this smooth component. Of course, some of these objects will be associated with galaxies, since the spatial distributions of GCs are often more extended than starlight. We therefore consider 50% to be an upper limit on the IGC fraction within this central region. More detailed modeling of the GC distributions of individual galaxies, and wider coverage to trace the profile of the smooth component to larger radii, would help to refine this estimate.

Our estimate of the background is based on the outer parts of the ACS/WFC image, but in the case of A1689 it is necessary to make a radial-dependent correction for the effect of cluster lensing (Blakeslee 1999). The gravitational field of A1689 affects the spatial and magnitude distributions of the background sources. Following the formalism of Broadhurst et al. (1995) in the absence of lensing, we expect a power-law distribution of background sources $N_{bg}(m) \approx N_0 10^{\beta m}$, where N_0 is a constant and β is the logarithmic slope of the counts. The lensing magnifies the brightness of the sources by the position-dependent magnification factor A, and thus shifts the source magnitudes brighter by 2.5 $\log(A)$. Lensing also increases the

surface area by the same factor, and thus decreases the surface density. As a result, the effect of the lens magnification can be approximated as

$$N'_{bg}(m) = A^{-1}\, N_0\, 10^{\beta(m+2.5\,\log A)} = N_{bg}(m)\, A^{-2.5(0.4-\beta)}, \quad (4)$$

where N'_{bg} is the observed (lensed) number density. Generally, $\beta < 0.4$, so the background counts over a fixed magnitude range are decreased, or diluted, by a factor $D = A^{-2.5(0.4-\beta)}$. The counts can also be amplified ($D > 1$) in regions where $A < 1$ (see Broadhurst et al. 1995 for a detailed discussion).

The magnification A depends on the distance and mass distribution of the lens, as well as the distance to the source plane. In general, A can be written as:

$$A = \frac{1}{|\,(1-\kappa)^2 - \gamma^2\,|}, \quad (5)$$

where κ and γ are the convergence and shear, respectively, for a given source distance. We use a non-parametric κ map for A1689 (M. J. Jee et al. 2013, in preparation; see also Jee et al. 2007) and, since we are calculating the number densities in circular annuli, we adopt the spherical approximation $\gamma = \bar{\kappa} - \kappa$, where $\bar{\kappa}$ is the mean convergence interior to the radius r. Taking $\beta = 0.35$ (e.g., Benítez et al. 2004), we finally derive the dilution factor D as a function of radius; the orange line in the right panel of Figure 5 represents the product of D and the background at large radius. The background level bg has been normalized to the outermost several bins; interior to this radius, the dilution is both negative and positive, depending on radius.

We note that Coe et al. (2010) also constructed a κ map for A1689 using their "LensPerfect" algorithm, and they reported the best-fitting Sérsic model parameters for the radially averaged profile. As a check, we derived a background source dilution profile using Coe et al.'s Sérsic parameters; the differences with respect to the above analysis were less than 1%.

Finally, we use the radial surface density distribution to correct for the incomplete area coverage (accounting for masked regions and incomplete outer annuli) out to a projected radius of 400 kpc (130″). This correction increases the sample of GC candidates to 10,596 and subtraction of the radial-dependent background contamination then produces a final sample of 8417 ± 1096 GC candidates with $I_{814} < 29.32$ and $r < 400$ kpc.

4. TOTAL GC NUMBER AND SPECIFIC FREQUENCY

After applying the corrections for incompleteness, partial area coverage, and background contamination, we ended up with a sample of 8417 GCs with $m < 29.32$ within $r < 400$ kpc of the central cD galaxy in A1689. To estimate the total size of the GC population, we assume that the GCLF is similar to those studied in massive ellipticals in more nearby clusters (e.g., Harris 2001; Jordán et al. 2007; Harris et al. 2009; Peng et al. 2009; Villegas et al. 2010). Based on these works, the absolute I_{814}-band GCLF turnover should occur at $M^{\rm TO}_{814} = -8.10 \pm 0.10$ AB mag. Including the distance modulus, Galactic extinction, and a K-correction in F814W of 0.03 mag (calculated for a GC spectrum at this redshift) implies an apparent turnover magnitude of 31.71 mag. However, the lookback time to $z = 0.183$ is 2.25 Gyr, and stellar population models (Bruzual & Charlot 2003) imply that old, metal-poor systems such as GCs would have been ∼0.15 mag more luminous at this epoch. This estimate is probably an upper limit because GC formation likely occurred earlier in A1689 than in local clusters

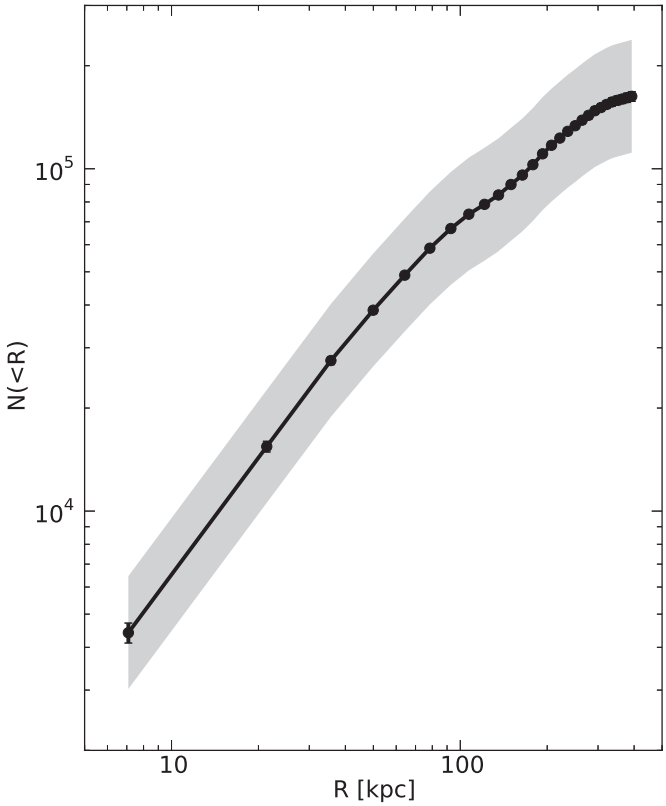

Figure 6. Cumulative radial profile of the total number of GCs, corrected for magnitude and area incompleteness and background contamination, then extrapolated over the GCLF. The gray region shows the uncertainty due to the GCLF parameters.

such as Virgo, Coma, or Fornax (see the related discussion in Villegas et al. 2010). We therefore adopt an apparent turnover magnitude $m^{\rm TO}_{814} = 31.6 \pm 0.2$ AB and use a Gaussian width $\sigma_{\rm LF} = 1.4 \pm 0.1$ mag.

The extrapolated total population of GCs within $r < 400$ kpc is then $N^{\rm total}_{\rm GC} = 162{,}850^{\pm 75450}_{\pm 51310}$. The main source of error is the uncertainty in the GCLF parameters; for instance, using $\sigma_{\rm LF} = 1.3$ increases $N^{\rm total}_{\rm GC}$ by 30%. Figure 6 shows the radial cumulative profile of $N_{\rm GC}$, including the uncertainty region. For comparison, based on the Next Generation Virgo Survey (Ferrarese et al. 2012), the total number of GCs within the same 400 kpc radius of M87 in the center of the nearby Virgo cluster is 26400 ± 3200 (P. Durrell et al., in preparation), a factor of six lower.

The specific frequency, S_N, is defined as

$$S_N = N_{\rm GC}\, 10^{0.4(M_V+15)}, \quad (6)$$

where M_V is the absolute magnitude of the galaxy in the V band and both $N_{\rm GC}$ and M_V are measured over the same physical region. Since our data are in I_{814}, we need to apply a photometric transformation to obtain M_V. The absolute magnitude M_V is derived as:

$$M_V = I_{814} - (m-M) - A_{814} - K_{814} + (V-I_{814}), \quad (7)$$

where $(m-M)$ is the distance modulus, A_{814} is the Galactic extinction, K_{814} is the K-correction, and $(V-I_{814})$ is the rest-frame color. We calculate $K_{814} = 0.11$ mag for the spectral energy distribution of a giant elliptical at $z = 0.183$, and based on the extensive compilation of $(V-I)$ galaxy colors

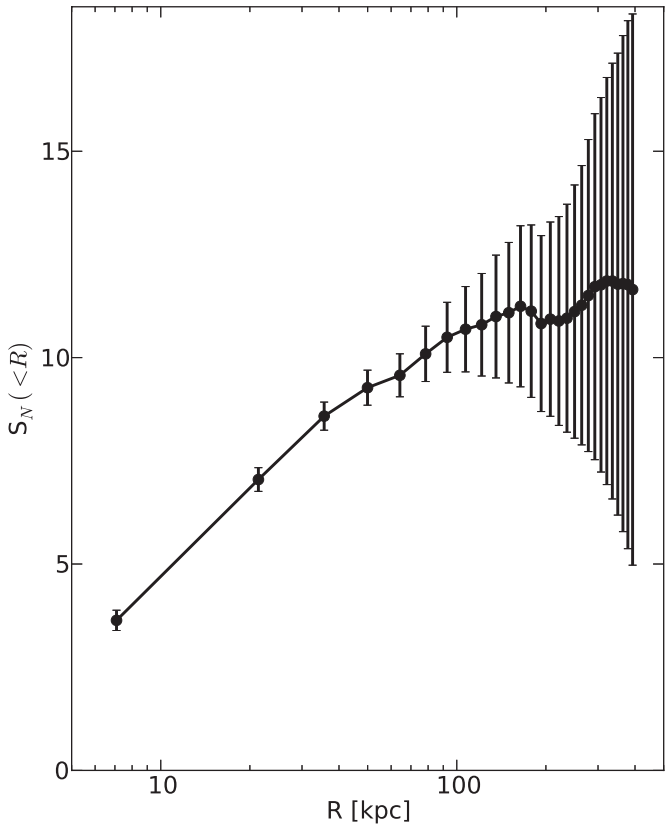

Figure 7. Cumulative specific frequency S_N as a function of radius; the error bars include statistical uncertainties in the number of GCs for the assumed (fixed) GCLF and the uncertainty in the galaxy light profile.

by Tonry et al. (2001), we adopt $(V-I_{814}) = 0.83$ (AB mag), in order to obtain M_V. Figure 7 shows the resulting cumulative S_N as a function of radius with the errors propagated from the GC counts and the galaxy luminosity. The uncertainty in the luminosity comes mainly from the assumed sky level $\mu_{814}^{\rm sky} = 20.90 \pm 0.01$ mag arcsec^{-2}, causing the size of the S_N error bars to increase strongly with radius.

For comparison to nearby galaxies, we need to consider how S_N would evolve over a lookback time of 2.25 Gyr. There is no significant star formation in the A1689 early-type galaxies that dominate this central field (Balogh et al. 2002) and stellar population models that match the colors of nearby giant ellipticals (e.g., 10 Gyr old, solar metallicity models of Bruzual & Charlot 2003) indicate that these objects have passively faded by about 0.20 mag since $z = 0.183$. Assuming negligible destruction of GCs over this time, the passive galaxy evolution will cause S_N to become 20% higher at $z = 0$ than at the observed epoch of A1689. Thus, the global value of $S_N = 11.7$ within 400 kpc would correspond to $S_N = 14.0$ at $z = 0$, after correcting for passive evolution, similar to the S_N values observed for the central cD galaxies in the nearby Virgo, Coma, and Hydra clusters (Tamura et al. 2006; Peng et al. 2008, 2011; Harris et al. 2009; Wehner et al. 2008). Of course, for a more exact comparison, the S_N values should be estimated on similar physical scales. Blakeslee (1999) measured S_N within apertures of 40 and 65 kpc for the cores of six rich Abell clusters; he reported $\langle S_N(40)\rangle = 8.7$ and $\langle S_N(65)\rangle = 9.2$ (with rms scatters of $\sim$2 in both cases). The corresponding values for A1689 at $z = 0$ are $S_N(40) = 10.6 \pm 0.4$ and $S_N(65) = 11.5 \pm 0.5$, near the high end of the observed range for nearby massive clusters.

In addition to the cumulative S_N, it is also worth considering the behavior of the local S_N. We have noted that the surface density distribution of GC candidates is not completely smooth, since GCs are preferentially located around bright galaxies. This clustering causes the "bump" at $\sim$1.′1 (200 kpc) in the GC radial density profile shown in Figure 5. This feature in the GC density profile corresponds to a grouping of bright galaxies at this radius, as highlighted within the green annulus in the right panel of Figure 8. However, since the GCs are not perfect tracers of the stellar light and their spatial concentrations are less sharply peaked than the galaxy profiles, an excess of galaxies at a given location tends to *decrease* the local value of S_N, if the galaxies have a "normal" $S_N \approx 4$. Therefore, at the same radius of 200 kpc where there is a "bump" in the number density of GCs, we actually find a "dip" in the local value of S_N, as shown by the green band in the left panel of Figure 8. A corresponding dip occurs near 200 kpc in the cumulative S_N distribution in Figure 7.

The scaling of $N_{\rm GC}$ in brightest cluster galaxies with the total underlying mass within a common projected radius has been interpreted as a consequence of an early universal GC formation efficiency in dense regions. Using the value 0.71 ± 0.22 GCs per $10^9\ M_\odot$ (Blakeslee 1999), our derived $N_{\rm GC}^{\rm total}$ would predict a total mass of $\sim 2.3 \times 10^{14}\ M_\odot$ within 400 kpc in A1689. However, this estimate depends on the GCs following the same radial profile as the total matter distribution. While observations indicate that their spatial distribution is more extended than the starlight, until now it has not been possible to test how GCs relate to the dark matter distribution. We explore these issues in the following section.

5. COMPARISON OF MASS PROFILES

With the goal of testing the existence of a universal GC formation efficiency in an extreme system such as A1689, we compare the amounts of mass in this central field in the form of GCs, stars, hot intracluster gas, and total mass (including dark matter). Figure 9 provides a two-dimensional visual comparison of the number density of GCs, the galaxy luminosity model, the lensing-derived mass distribution, and the X-ray emission map. The symmetry and smoothness of the X-ray gas stand out; this effect is not due to resolution, as evidenced by the compactness of the X-ray point sources in the image. To make quantitative comparisons, we now derive the projected radial mass distributions for each component.

For the GCs, the total number within 400 kpc calculated in the preceding section can be converted to a mass by assuming a mean individual GC mass of $\langle \mathcal{M}_{\rm GC}\rangle = 2.4 \times 10^5\ M_\odot$ (McLaughlin 1999; Blakeslee 1999). The estimated total mass in GCs within this radius is therefore $\mathcal{M}_{\rm GC}^{\rm total} = 3.9 \times 10^{10}\ M_\odot$. For perspective, this value is 60%–80% of the total stellar mass of the Milky Way galaxy (Flynn et al. 2006; McMillan 2011).

To calculate the stellar mass $\mathcal{M}_\star$, we assume a stellar mass-to-light ratio $\mathcal{M}_\star/L_V = 4$, based on solar metallicity Bruzual & Charlot (2003) models with a Salpeter initial mass function (IMF). Of course, the assumption of a constant $\mathcal{M}_\star/L_V$ at all radii is a first-order approximation. Moreover, the $\mathcal{M}_\star/L_V$, and thus the derived mass, can vary by $\sim$30%, depending on the IMF, but the choice of a Salpeter IMF is reasonable for early-type galaxies (e.g., van Dokkum & Conroy 2010; Conroy & van Dokkum 2012). Finally, using $M_{V,\odot} = 4.81$, we obtain $\mathcal{M}_\star^{\rm total} = 4.7 \times 10^{12}\ M_\odot$.

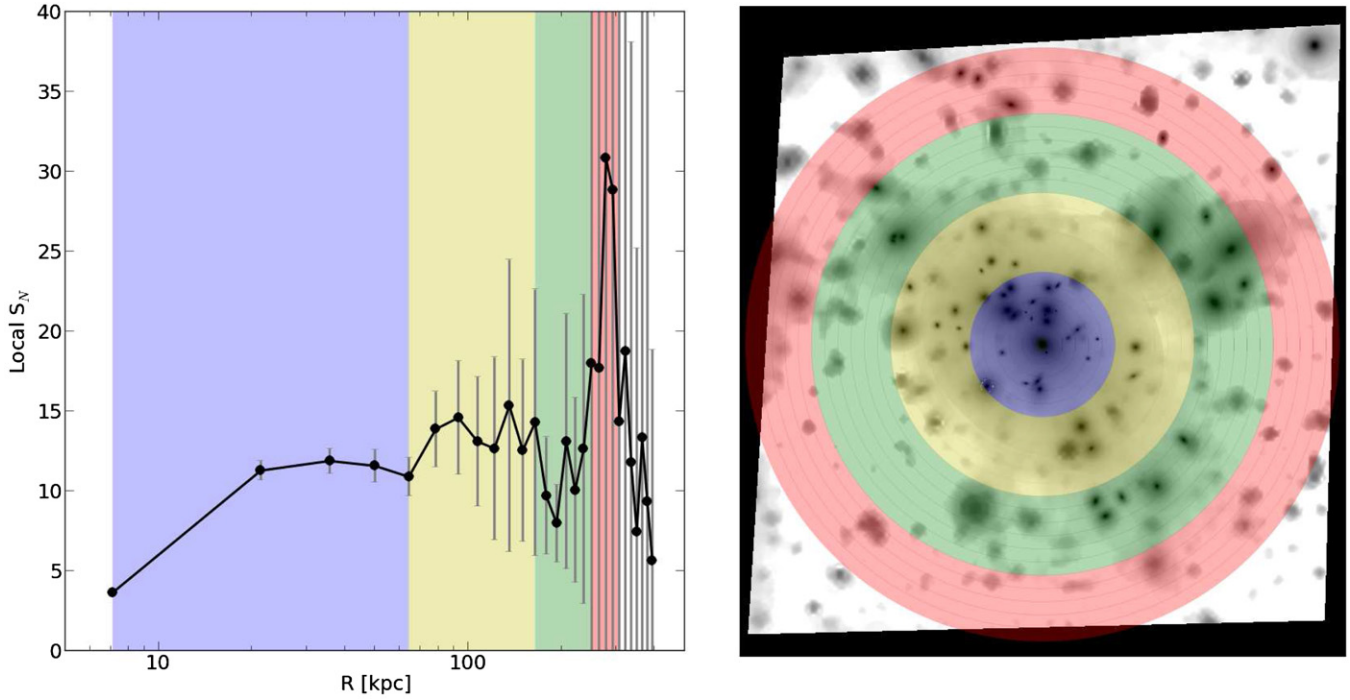

Figure 8. Left panel: local S_N within $\sim 5''$ annuli as a function of radius. Right panel: galaxy light model. In both panels, the blue, yellow, green and red regions indicate radial ranges of 0–70, 70–180, 180–230, and 230–300 kpc, respectively. The "dip" in the local S_N at $R \approx 200$ kpc is caused by the grouping of bright galaxies within the green annulus.

(A color version of this figure is available in the online journal.)

The X-ray gas mass was estimated from the three-dimensional gas density profile $\rho_g(r)$ constructed by Lemze et al. (2008) based on *Chandra* X-ray data. We found that the published $\rho_g(r)$ is well fit by a function of the form

$$\rho_g(r) = \frac{\rho_0}{[1 + (r/r_0)^\alpha]^\beta}, \quad (8)$$

with best-fit values $\rho_0 = 2.1 \times 10^{-25}$ g cm^{-3}, $r_0 = 321$ kpc, $\alpha = 0.58$, and $\beta = 5.6$ (giving $r^{-\alpha\beta} \sim r^{-3.2}$ at large r). These parameters are only used for interpolating the X-ray data points. We then integrate this function along the line of sight ℓ to obtain the projected gas mass surface density ζ as

$$\zeta = 2\int_0^{1\,\mathrm{Mpc}} \rho(\sqrt{R^2 + \ell^2})d\ell, \quad (9)$$

where R is the projected radius. This calculation gives an X-ray gas mass within 400 kpc of $\mathcal{M}^{\mathrm{total}}_{\mathrm{X-ray}} = 3.6 \times 10^{13}\, M_\odot$. The baryonic mass comprises field stars, GCs, and intracluster gas. Adding all the components, we obtain $\mathcal{M}_{\mathrm{baryon}} \approx 4.1 \times 10^{13}\, M_\odot$.

The total mass, $\mathcal{M}_{\mathrm{total}}$, is estimated from the κ map used previously in Section 3.5. It includes both baryonic and non-baryonic mass, but is dominated by the non-baryonic component (at least outside the central few kpc). The convergence κ is the mass surface density, normalized by the critical surface density (i.e., $\kappa = \Sigma/\Sigma_{\mathrm{crit}}$), where

$$\Sigma_{\mathrm{crit}} = \frac{c^2 D_s}{4\pi G D_L D_{Ls}}. \quad (10)$$

In the above equation, c is the speed of light, and D_L, D_s, and D_{Ls} are the distance to the lens (A1689), the distance to a reference source (assumed $z = 3$), and the distance from the lens to the source, respectively. Integrating, we find $\mathcal{M}_{\mathrm{total}} = 6.4 \times 10^{14}\, M_\odot$ within 400 kpc.

Figure 10 presents the radial mass density and cumulative mass profiles for each of the above components. The stars and GCs are strongly concentrated in and around the galaxies; the most prominent feature is the "bump" at $R \approx 200$ kpc, discussed above. The hot X-ray emitting gas and total mass exhibit much smoother profiles. The hot gas dominates the baryonic mass beyond the central $\sim$30 kpc.

To investigate the radial run of the GC mass fraction relative to the other mass components, we plot in Figure 11 the mass ratios for all possible combinations of the components in Figure 10. The stellar mass fraction in GCs ($\mathcal{M}_{GC}/\mathcal{M}_\star$, panel (f)) increases by a factor of $\sim$2.5 within the central 80 kpc and then levels off, consistent with the S_N profile shown previously. However, compared to either the X-ray gas or total matter, the GC mass fraction decreases as a function of radius (panels (b) and (a), respectively); the mass fraction in stars (panels (d) and (c)) shows a similar, even steeper, decline. As found in previous studies, the gas mass fraction (panel (e)) appears to increase monotonically with radius. Interestingly, the baryonic mass fraction (ratio of baryons to total mass, panel (g)) reaches a minimum near 150 kpc because the stellar mass is more concentrated than the dark matter but the gas is more extended. This quantity has been studied extensively in galaxy clusters as an approximation to the baryonic mass fraction of the universe ($\mathcal{M}_b/\mathcal{M}_{\mathrm{DM}} \sim \Omega_{\mathrm{b}}/\Omega_{\mathrm{DM}}$). For instance, Lin et al. (2012) measured baryon fractions for 94 galaxy clusters over a wide range redshift; our value for A1689 in Figure 11 agrees well with the results of this recent study.

McLaughlin (1999) derived an average efficiency of GC formation per baryonic mass, i.e., $\epsilon_b = \mathcal{M}_{\mathrm{GC}}/\mathcal{M}_{\mathrm{baryon}}$, of

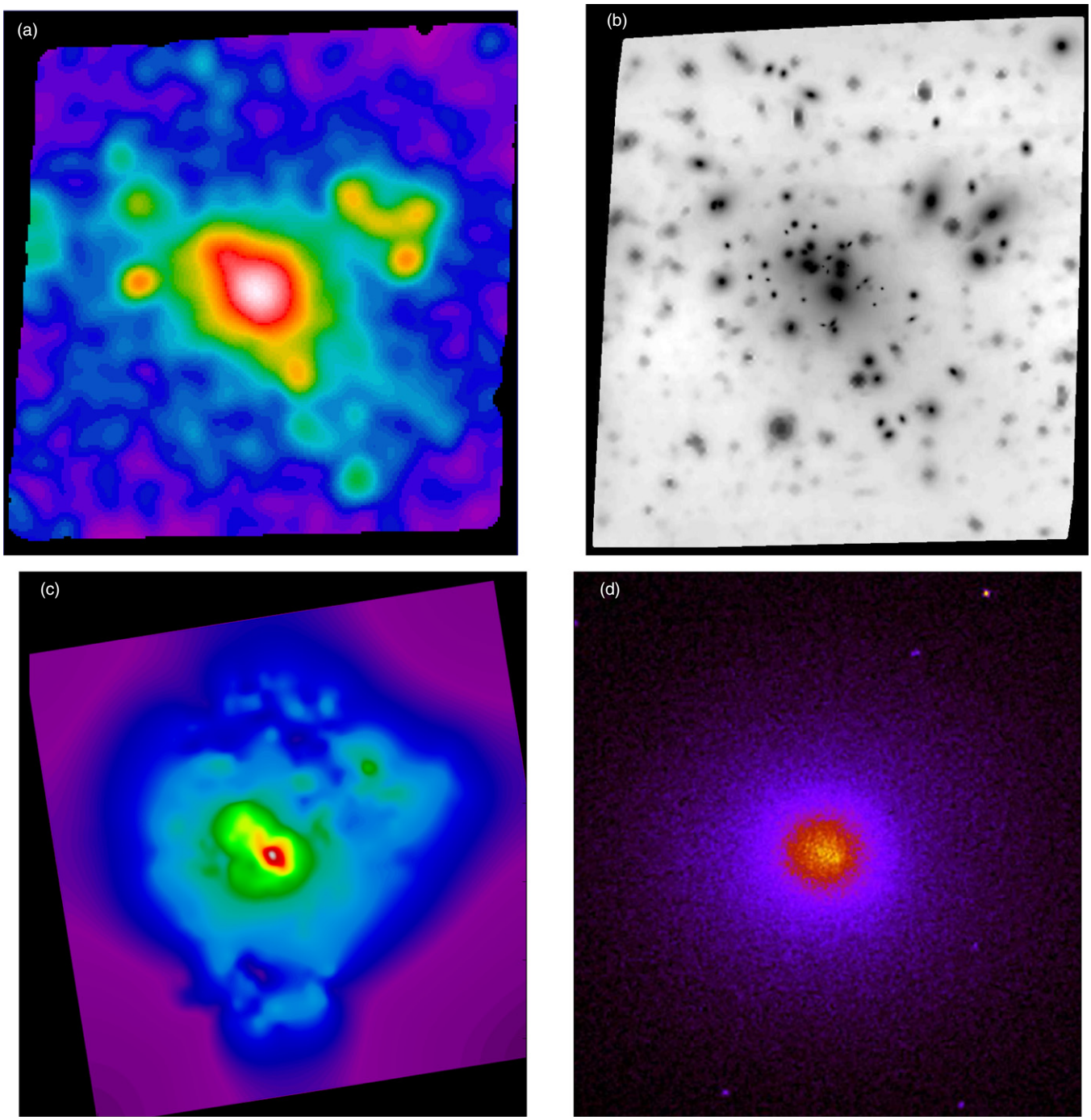

Figure 9. (a) Surface number density of GC candidates, smoothed with a Gaussian of FWHM = 10″ (300 pixels); (b) surface brightness distribution from 59 galaxies with isophotal models plus the SExtractor background map; (c) lensing-derived total surface mass density (includes baryonic and non-baryonic components); (d) X-ray surface brightness distribution (from the *Chandra* archive).

(A color version of this figure is available in the online journal.)

0.0026 within $r < 100$ kpc. Comparing McLaughlin's value with our estimate for the same radial range (Figure 11(h)), we find $\epsilon_b = 0.0021$, which is within the scatter of the values found by McLaughlin. Meanwhile, Blakeslee (1999) reported a mean efficiency per total mass of $\epsilon_t = \mathcal{M}_{\rm GC}/\mathcal{M}_{\rm total} = 1.7 \times 10^{-4}$ within $r < 50$ kpc; within this radius, we obtain $\epsilon_t = 1.8 \times 10^{-4}$ (Figure 11(a)), in close agreement with the expected value. However, although the mass ratios within these relatively small radii are remarkably consistent with the "universal" efficiencies previously proposed in the literature, the global values are not. Within 400 kpc, we find $\epsilon_b^{A1689} = 0.00095$ and $\epsilon_t^{A1689} = 6.1 \times 10^{-5}$, both a factor of three lower than the values cited above. After converting to our assumed mean GC mass, the results of Spitler & Forbes (2009) imply $\epsilon_t = 4.2 \times 10^{-5}$, about 30% lower than our value within 400 kpc but consistent within the errors; however, it not clear what radius to use in this case. Thus, we emphasize again the importance of comparing such ratios within the same physical radii.

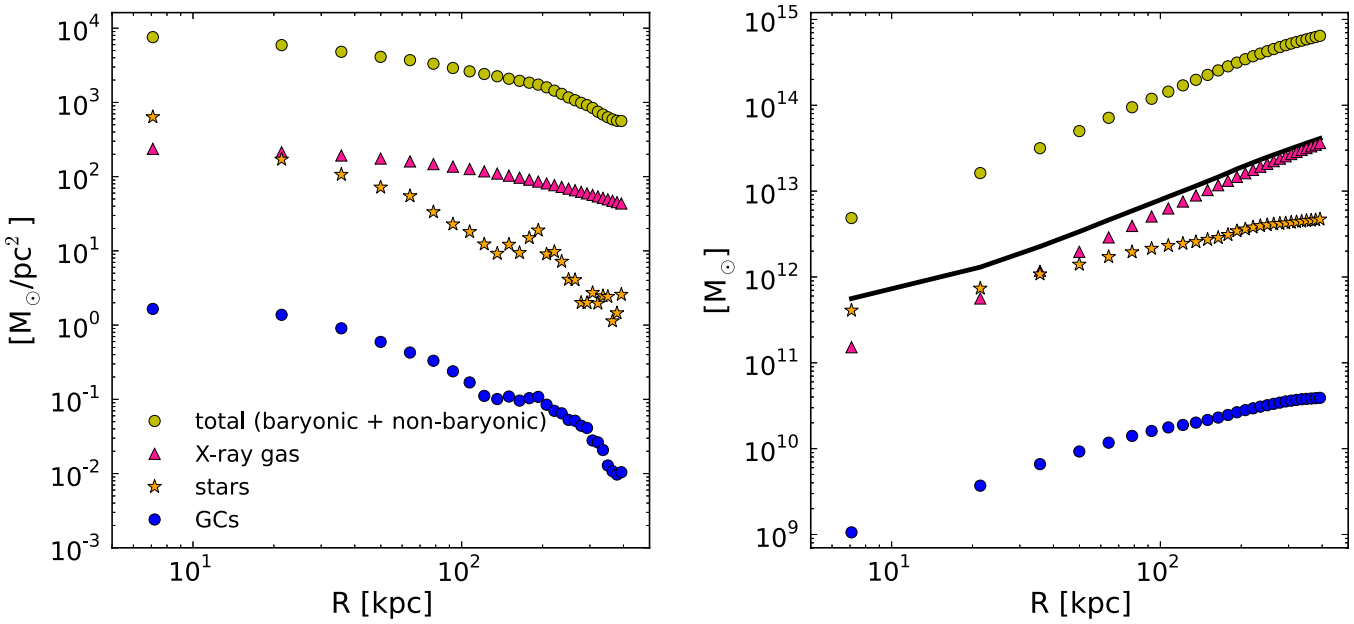

Figure 10. Left: radial mass density profile for each component. Right: cumulative mass profiles vs. radius. The thick black line indicates the cumulative profile for the baryonic mass, $\mathcal{M}_{\rm baryon} = \mathcal{M}_{\rm X-ray} + \mathcal{M}_{\star}$.

(A color version of this figure is available in the online journal.)

6. DISCUSSION AND CONCLUSIONS

Deep broadband imaging with *HST*/ACS ($\gtrsim$90% complete to $I_{814} = 29$) has revealed an extremely rich GC system in the center of the massive lensing cluster A1689. The estimated total population of $162{,}850^{+75{,}450}_{-51{,}310}$ GCs within a projected radius of 400 kpc represents the largest system of GCs studied to date, six times the number within the same radius in the Virgo cluster. The large error bars are due to the uncertainty in the GCLF parameters. Although the Gaussian form of the GCLF is well calibrated for giant ellipticals in rich clusters, even with 20.9 hr of integration, our data fall 1.6σ short of the GCLF turnover; we therefore sample only 10% of the GCs brighter than the turnover (or 5% of the total population, assuming a symmetric GCLF). Thus, the large extrapolation yields a sizable systematic uncertainty. Nevertheless, this system remains the largest GC population yet discovered, with at least a factor of two more GCs than the next most populous systems, including Coma and A3558 (Peng et al. 2011; Barber DeGraaff 2011).

Our analysis accounts for the effects of the Eddington bias, gravitational magnification of the background surface density, redshifting of the bandpass (*K*-corrections), and passive evolution of the GCLF. Although it is possible that there has been some evolution in the shape of the GCLF since $z = 0.18$, this evolution would mainly occur from the destruction of low-mass GCs (e.g., Jordán et al. 2007; McLaughlin & Fall 2008) with little effect on the masses of objects near the GCLF peak or brighter. Our assumption of a symmetric GCLF would therefore likely underestimate the population at $z = 0.18$, but the additional low-mass GCs would have little effect on our total mass estimates.

The spatial distribution of GC candidates in the center of A1689 is not completely smooth; there are obvious concentrations around the cluster galaxies. However, by masking the bright and intermediate-luminosity galaxies, we can trace an apparently smooth component, which comprises half of the total population when integrated over the field (via the best-fit Sérsic model). If we identify these objects as belonging to a possible intracluster population of GCs, then there may be as many as ~80,000 such IGCs within the central 400 kpc in A1689. We consider this number an upper limit, since some of these IGC candidates are undoubtedly bound to individual galaxies. We plan to refine our estimate of the IGC population by modeling the GC distributions around individual galaxies. Imaging to a similar depth at larger radii from the cluster center would also help in constraining the IGC population.

The cumulative S_N increases from a value near 5 within 10 kpc to 10 ± 0.5 (not including systematic uncertainty from the GCLF) within 70 kpc. Although the uncertainties in S_N become large beyond 100 kpc, the profile appears to flatten and the value within 150 kpc is $S_N = 11.1 \pm 2.0$. There is a clear dip in the cumulative S_N around 200 kpc, before it rises again to ~12 within 300 kpc. The dip at 200 kpc occurs despite a local increase in the GC number density at the same radius; it is caused by a subgrouping of several bright galaxies that appear to have a more normal $S_N < 10$ (as was shown by comparing the green regions in Figure 8). Such galaxies contribute relatively more to the denominator of S_N than to the numerator. This fact highlights that cannibalization of normal cluster galaxies by the central cD will tend to decrease S_N, rather than increase it; thus the high S_N value must have been imprinted in the cluster core at early times. We have also noted that passive evolution of the galaxy luminosity since $z = 0.18$ would cause the observed S_N to increase by 20% at $z = 0$, but even with this effect, the high S_N in A1689 would not be anomalous among cD galaxies in local clusters.

Remarkably, the mass in GCs within 400 kpc of the center of A1689 is equivalent to 60%–80% of the total stellar mass of the Milky Way. Integrated out to the virial radius of ~3 Mpc, the total mass in GCs is likely twice that of the stars in our Galaxy. Of course, this mass represents only a small fraction of the total mass in A1689. We have examined the mass profile of the GCs as a function of radius and compared it with the mass profiles of the stellar light, hot intracluster gas, and total lensing-derived

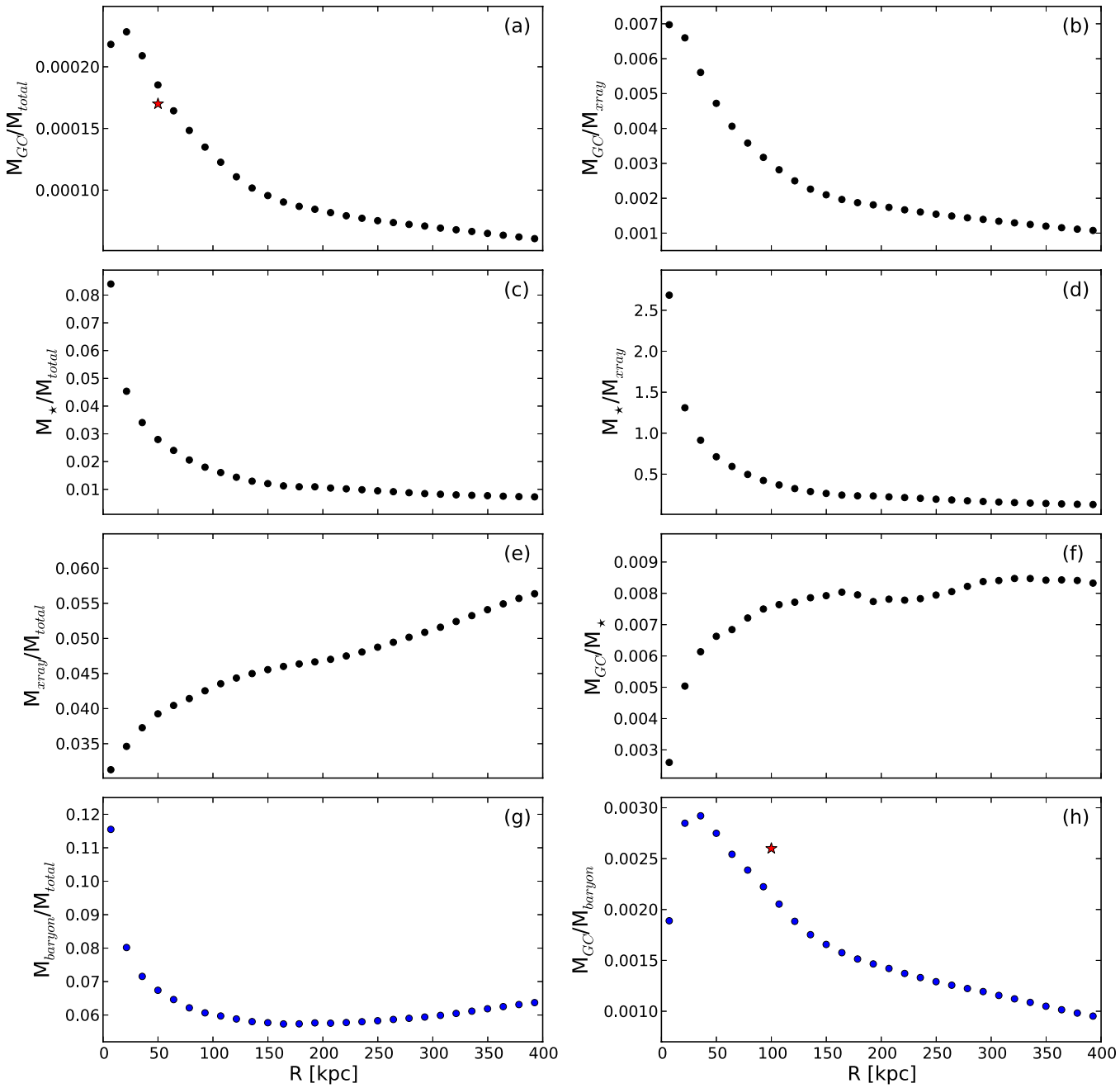

Figure 11. Ratios of the cumulative distributions for various mass components in A1689, based on the curves plotted in Figure 10. The red stars in (a) and (h) represent the values $\epsilon_t = 1.7 \times 10^{-4}$ from Blakeslee (1999) and $\epsilon_b = 0.0026$ from McLaughlin (1999), respectively. See the text for a discussion. Note that the GC stellar mass fraction $\mathcal{M}_{\rm GC}/\mathcal{M}_{\star}$ shown in panel (f) is equivalent to $S_{\mathcal{M}}/100$, where $S_{\mathcal{M}}$ is the "specific mass" parameter used in some studies (e.g., Peng et al. 2008).
(A color version of this figure is available in the online journal.)

matter content within this central field. The mass profile of the GCs is somewhat more extended than the stellar light, but more concentrated than the hot gas or dark matter. If the mass fraction is viewed as a GC formation efficiency, then the efficiency (in terms of either baryonic or total mass) decreases as a function of radius and there is no "universal" value.

On the other hand, when compared within the same physical radii, the GC mass fractions with respect to the total and baryonic masses agree with the values found in samples of nearby clusters, all of which have masses lower than A1689. This result suggests the possibility of a universal GC formation profile within galaxy clusters. In contrast, Laganá et al. (2011) estimated the stellar, intracluster gas, and total masses within r_{500} for 19 galaxy clusters and found a decrease in the stellar mass fraction with increasing total mass of the system. That is, more massive clusters had lower overall star formation efficiencies. Taken together, these results are consistent with the view that the high S_N values in cD galaxies are a consequence of "missing" stellar light in more massive clusters (Blakeslee 1997), rather than an excess in the number of GCs.

Finally, we note that in a recent study, Suárez-Madrigal et al. (2012) modeled the influence of the dark matter halo on molecular clouds at different locations within the halo. They found that the star formation efficiency of the clouds depends on the ambient density, and thus decreases with distance from the halo center, in qualitative agreement with our finding that GC

formation efficiency decreases with radius. If the mass density profiles in galaxy clusters are approximately universal (e.g., Navarro et al. 1997), then it would also make sense that the GC formation efficiency profile may follow a universal form. Further studies of the GC, baryonic, and total mass profiles in galaxy clusters are needed to test this intriguing possibility.

Support for program GO-11710 was provided in part through a grant from the Space Telescope Science Institute, which is operated by the Association of Universities for Research in Astronomy, Inc., under NASA contract NAS5-26555. We thank Dan Magee for help with the CTE correction software. J.P.B. acknowledges helpful conversation with James Bullock. K.A.A.-M. acknowledges the support of CONACyT (Mexico). This research has made use of the NASA/IPAC Extragalactic Database (NED), which is operated by the Jet Propulsion Laboratory, California Institute of Technology, under contract with NASA.

Facility: HST (ACS/WFC)

REFERENCES

Abadi, M. G., Navarro, J. F., & Steinmetz, M. 2006, MNRAS, 365, 747
Abell, G. O., Corwin, H. G., Jr., & Olowin, R. P. 1989, ApJS, 70, 1
Alamo-Martínez, K. A., West, M. J., Blakeslee, J. P., et al. 2012, A&A, 546, A15
Anderson, J., & Bedin, L. R. 2010, PASP, 122, 1035
Andersson, K. E., & Madejski, G. M. 2004, ApJ, 607, 190
Balogh, M. L., Couch, W. J., Smail, I., Bower, R. G., & Glazebrook, K. 2002, MNRAS, 335, 10
Barber DeGraaff, R. G. 2011, PhD thesis, Washington State Univ.
Benítez, N., Ford, H., Bouwens, R., et al. 2004, ApJS, 150, 1
Bertin, E., & Arnouts, S. 1996, A&AS, 117, 393
Blakeslee, J. P. 1997, ApJL, 481, L59
Blakeslee, J. P. 1999, AJ, 118, 1506
Blakeslee, J. P. 2005, HiA, 13, 171
Blakeslee, J. P., Anderson, K. R., Meurer, G. R., Benítez, N., & Magee, D. 2003, in ASP Conf. Ser. 295, Astronomical Data Analysis Software and Systems XII, ed. H. E. Payne, R. I. Jedrzejewski, & R. N. Hook (San Francisco, CA: ASP), 257
Blakeslee, J. P., Tonry, J. L., & Metzger, M. R. 1997, AJ, 114, 482
Broadhurst, T., Benítez, N., Coe, D., et al. 2005, ApJ, 621, 53
Broadhurst, T. J., Taylor, A. N., & Peacock, J. A. 1995, ApJ, 438, 49
Brodie, J. P., & Strader, J. 2006, ARA&A, 44, 193
Bruzual, G., & Charlot, S. 2003, MNRAS, 344, 1000
Chies-Santos, A. L., Larsen, S. S., & Kissler-Patig, M. 2012, MNRAS, 427, 2349
Chies-Santos, A. L., Larsen, S. S., Kuntschner, H., et al. 2011, A&A, 525, A20
Cho, J., Sharples, R. M., Blakeslee, J. P., et al. 2012, MNRAS, 422, 3591
Coe, D., Benítez, N., Broadhurst, T., & Moustakas, L. A. 2010, ApJ, 723, 1678
Cohen, J. G., Blakeslee, J. P., & Côté, P. 2003, ApJ, 592, 866
Cohen, J. G., Blakeslee, J. P., & Ryzhov, A. 1998, ApJ, 496, 808
Conroy, C., & van Dokkum, P. G. 2012, ApJ, 760, 71
Conroy, C., & Wechsler, R. H. 2009, ApJ, 696, 620
Côté, P., Blakeslee, J. P., Ferrarese, L., et al. 2004, ApJS, 153, 223
De Lucia, G., & Helmi, A. 2008, MNRAS, 391, 14
De Lucia, G., Springel, V., White, S. D. M., Croton, D., & Kauffmann, G. 2006, MNRAS, 366, 499
Eddington, A. S. 1913, MNRAS, 73, 359
Ferrarese, L., Côté, P., Cuillandre, J.-C., et al. 2012, ApJS, 200, 4
Flynn, C., Holmberg, J., Portinari, L., Fuchs, B., & Jahreiß, H. 2006, MNRAS, 372, 1149
Font, A. S., Johnston, K. V., Bullock, J. S., & Robertson, B. E. 2006, ApJ, 638, 585
Ford, H. C., Clampin, M., Hartig, G. F., et al. 2003, Proc. SPIE, 4854, 81
Ford, H. C., Illingworth, G. D., Clampin, M., et al. 2002, BAAS, 34, 675
Fruchter, A. S., & Hook, R. N. 2002, PASP, 114, 144
Georgiev, I. Y., Puzia, T. H., Goudfrooij, P., & Hilker, M. 2010, MNRAS, 406, 1967
Girardi, M., Fadda, D., Escalera, E., et al. 1997, ApJ, 490, 56
Graham, A. W., & Driver, S. P. 2005, PASA, 22, 118
Guo, Q., White, S., Li, C., & Boylan-Kolchin, M. 2010, MNRAS, 404, 1111
Harris, W. E. 1991, ARA&A, 29, 543
Harris, W. E. 2001, in Star Clusters, Saas-Fee Advanced Courses, Vol. 28, ed. L. Labhardt & B. Binggeli (Berlin: Springer), 223
Harris, W. E., Kavelaars, J. J., Hanes, D. A., Pritchet, C. J., & Baum, W. A. 2009, AJ, 137, 3314
Harris, W. E., Pritchet, C. J., & McClure, R. D. 1995, ApJ, 441, 120
Harris, W. E., & van den Bergh, S. 1981, AJ, 86, 1627
Hinshaw, G., Larson, D., Komatsu, E., et al. 2012, arXiv:1212.5226
Jedrzejewski, R. I. 1987, MNRAS, 226, 747
Jee, M. J., Ford, H. C., Illingworth, G. D., et al. 2007, ApJ, 661, 728
Johnston, K. V., Bullock, J. S., Sharma, S., et al. 2008, ApJ, 689, 936
Jordán, A., Blakeslee, J. P., Peng, E. W., et al. 2004, ApJS, 154, 509
Jordán, A., McLaughlin, D. E., Côté, P., et al. 2007, ApJS, 171, 101
Jordán, A., West, M. J., Côté, P., & Marzke, R. O. 2003, AJ, 125, 1642
Komatsu, E., Smith, K. M., Dunkley, J., et al. 2011, ApJS, 192, 18
Kruijssen, J. M. D. 2012, MNRAS, 426, 3008
Laganá, T. F., Zhang, Y.-Y., Reiprich, T. H., & Schneider, P. 2011, ApJ, 743, 13
Lee, M. G., Park, H. S., & Hwang, H. S. 2010, Sci, 328, 334
Lemze, D., Barkana, R., Broadhurst, T. J., & Rephaeli, Y. 2008, MNRAS, 386, 1092
Lemze, D., Broadhurst, T., Rephaeli, Y., Barkana, R., & Umetsu, K. 2009, ApJ, 701, 1336
Limousin, M., Richard, J., Jullo, E., et al. 2007, ApJ, 668, 643
Lin, Y.-T., Stanford, S. A., Eisenhardt, P. R. M., et al. 2012, ApJL, 745, L3
McLaughlin, D. E. 1999, AJ, 117, 2398
McLaughlin, D. E., & Fall, S. M. 2008, ApJ, 679, 1272
McLaughlin, D. E., Harris, W. E., & Hanes, D. A. 1994, ApJ, 422, 486
McMillan, P. J. 2011, MNRAS, 414, 2446
Mieske, S., Infante, L., Benítez, N., et al. 2004, AJ, 128, 1529
Moore, B., Diemand, J., Madau, P., Zemp, M., & Stadel, J. 2006, MNRAS, 368, 563
Navarro, J. F., Frenk, C. S., & White, S. D. M. 1997, ApJ, 490, 493
Peng, E. W., Ferguson, H. C., Goudfrooij, P., et al. 2011, ApJ, 730, 23
Peng, E. W., Jordán, A., Blakeslee, J. P., et al. 2009, ApJ, 703, 42
Peng, E. W., Jordán, A., Côté, P., et al. 2008, ApJ, 681, 197
Puzia, T. H., Kissler-Patig, M., Thomas, D., et al. 2005, A&A, 439, 997
Schlafly, E. F., & Finkbeiner, D. P. 2011, ApJ, 737, 103
Sereno, M., Ettori, S., Umetsu, K., & Baldi, A. 2013, MNRAS, 428, 2241
Sérsic, J. L. 1968, Atlas de Galaxias Australes (Cordoba: Observatorio Astronomico)
Sirianni, M., Jee, M. J., Benítez, N., et al. 2005, PASP, 117, 1049
Spitler, L. R., & Forbes, D. A. 2009, MNRAS, 392, L1
Springel, V., White, S. D. M., Jenkins, A., et al. 2005, Natur, 435, 629
Stetson, P. B. 1987, PASP, 99, 191
Suárez-Madrigal, A., Ballesteros-Paredes, J., Colín, P., & D'Alessio, P. 2012, ApJ, 748, 101
Tamura, N., Sharples, R. M., Arimoto, N., et al. 2006, MNRAS, 373, 588
Taylor, A. N., Dye, S., Broadhurst, T. J., Benitez, N., & van Kampen, E. 1998, ApJ, 501, 539
Teague, P. F., Carter, D., & Gray, P. M. 1990, ApJS, 72, 715
Tody, D. 1986, Proc. SPIE, 627, 733
Tody, D. 1993, in ASP Conf. Ser. 52, Astronomical Data Analysis Software and Systems II, ed. R. J. Hanisch, R. J. V. Brissenden, & J. Barnes (San Francisco, CA: ASP), 173
Tonry, J. L., Dressler, A., Blakeslee, J. P., et al. 2001, ApJ, 546, 681
Tyson, J. A., & Fischer, P. 1995, ApJL, 446, L55
van den Bosch, F. C., Yang, X., Mo, H. J., et al. 2007, MNRAS, 376, 841
van Dokkum, P. G., & Conroy, C. 2010, Natur, 468, 940
Villegas, D., Jordán, A., Peng, E. W., et al. 2010, ApJ, 717, 603
Wehner, E. M. H., Harris, W. E., Whitmore, B. C., Rothberg, B., & Woodley, K. A. 2008, ApJ, 681, 1233
West, M. J., Cote, P., Jones, C., Forman, W., & Marzke, R. O. 1995, ApJL, 453, L77
West, M. J., Côté, P., Marzke, R. O., & Jordán, A. 2004, Natur, 427, 31
West, M. J., Jordán, A., Blakeslee, J. P., et al. 2011, A&A, 528, A115
Zekser, K. C., White, R. L., Broadhurst, T. J., et al. 2006, ApJ, 640, 639